Zhou *et al. Biochar* (2023) 5:10
https://doi.org/10.1007/s42773-023-00211-3

Biochar

ORIGINAL RESEARCH

Open Access

Experimental and numerical investigations of biochar-facilitated Cd^{2+} transport in saturated porous media: role of solution pH and ionic strength

Dan Zhou[1,2], Xingyue Bao[1], Zhe Chen[3], Rui Liu[3], Mingzheng Huang[1], Yonglian Xia[1], Chao Li[1] and Yi Huang[1,2*]

Abstract

The nanoscale biochar (N-BC) generated during the production and weathering of bulk biochar has caused significant concerns for its cotransport with contaminants spreading the contamination. In this study, the cotransport behaviors of N-BC with Cd^{2+} under variable solution chemistry were investigated for the first time, which can pose environmental contamination risks but have received little attention. The column experiment results showed that increasing ionic strength (IS) or decreasing pH retarded the transport of N-BC but promoted the transport of Cd^{2+} in their individual transport. In cotransport scenarios, Cd^{2+} facilitated the deposition of N-BC on the quartz sand with increasing IS or decreasing pH by providing additional sorption sites and led to the ripening of N-BC via cation bridging. N-BC retarded the transport of Cd^{2+} under all conditions. However, lower pH and higher IS could facilitate the release of Cd^{2+} from the immobile N-BC. The cotransport modeling results demonstrated that the Cd^{2+} adsorption on and desorption from the immobile N-BC controlled the retention and release of Cd^{2+} under variable pH and IS, while the influence of mobile N-BC on Cd^{2+} transport was minor. This study provided new insight for evaluating the potential contamination-spreading risks and suggested that rational use of biochar with great caution is necessary.

Highlights

- The presence of N-BC retarded the transport of Cd^{2+} under all conditions.
- Lower pH and higher IS could facilitate the release of Cd^{2+} from the immobile N-BC.
- The interaction of Cd^{2+} with the immobile N-BC controlled the transport of Cd^{2+}.

Keywords Nanoscale biochar, Cadmium, Cotransport, Numerical modeling

Handling Editor: Bin Gao

*Correspondence:
Yi Huang
huangyi@cdut.edu.cn
Full list of author information is available at the end of the article

Graphical Abstract

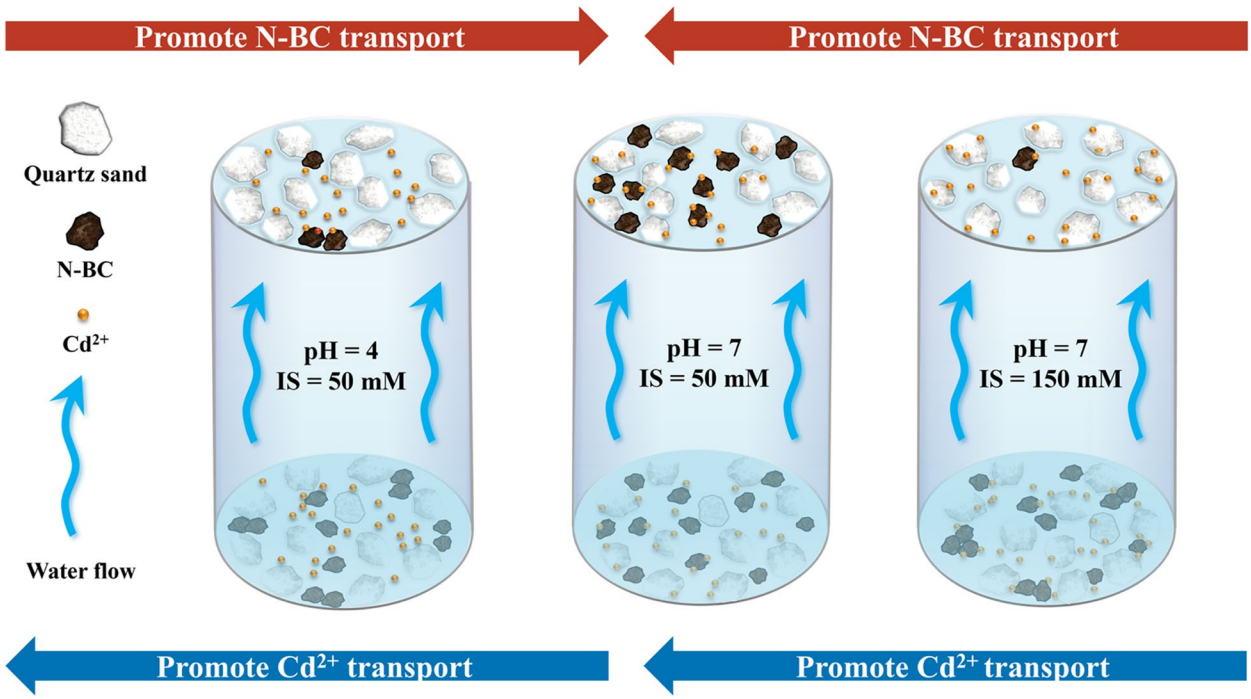

1 Introduction

Biochar is produced via biomass pyrolysis and is rich in carbon and functional groups, which has raised increasing attention due to its multiple environmental functions, such as carbon sequestration and pollutant adsorption (Beesley et al. 2011; Lehmann et al. 2011; Lu et al. 2012; Woolf et al. 2010). Besides bulk biochar, nanoscale biochar (N-BC) has also received growing concerns for its potential environmental risks. N-BC can be formed by matrix fracture and pore collapse of bulk biochar during charring, grinding, and sonication, or weathering in the natural environment releasing fine biochar particles, subject to soil hydrology, solution chemistry, and climate (Kuzyakov et al. 2014; Liu et al. 2018; Spokas et al. 2014; Xu et al. 2017). The generated N-BC can migrate in soils and aquifers, eventually reaching the ocean via river and atmosphere (Qu et al. 2016). The potential environmental risk of N-BC originates from not only its transport in the subsurface releasing harmful internal components simultaneously (e.g., heavy metals, polycyclic aromatic hydrocarbons, and dioxins), but also from facilitating the transport of contaminants by acting as a carrier (Cao et al. 2021; Tong et al. 2020; Xiang et al. 2021; Zhu et al. 2021). The mobility of N-BC in laboratory and field scale has been conducted with great effort (Chen et al. 2017; Wang et al. 2019; Yang et al. 2020b). Physicochemical conditions such as solution chemistry, biochar property, flow velocity, and porous media were all reported to pose significant impacts on the mobility of biochar via altering the electrical double layer thickness, surface functional groups, collision efficiency, and straining (Shang et al. 2013; Wang et al. 2013a; Zhang et al. 2010). The coexisting substances of metals (Cao et al. 2021; Jin et al. 2020), microplastics (Tong et al. 2020; Wang et al. 2022), organic matters (Yang et al. 2017, 2019; Zhu et al. 2021), and soil colloids (Gui et al. 2021) have also been verified to pose significant effects on the N-BC mobility in porous media via forming homo-/hetero-aggregates altering the surface charge density, aggregate size and steric repulsion of N-BC.

Cd^{2+} is a highly toxic and mobile heavy metal that mainly exists as a divalent ion in soils and water (Roberts 2014; Wang et al. 2021a, b; Zhang et al. 2020), which can be absorbed and accumulated in crops to the food chain. Multiple remediation methods were employed to remove or reduce the bioavailability of Cd^{2+} from soils, such as adsorption, precipitation, electrokinetic remediation, and bioremediation (Debrassi et al. 2012; Robinson et al. 2001; Yu et al. 2013). Among these methods, immobilizing Cd^{2+} in soils with biochar has attracted

growing interest for its simple operation, eco-safe, and low cost (Huang et al. 2015, 2017). Different forms of biochar were innovated to immobilize Cd^{2+} from soils, including pristine biochar (e.g., derived from rice straw (Tan et al. 2020), green peppers (Sun et al. 2020), poultry manure (Haider et al. 2021), metal/metal-oxide modified biochar (e.g., Fe, Fe_3O_4, and MgO modified (Tang et al. 2020a, b; Wan et al. 2020; Wang et al. 2021a, b), and other substance-amended biochar (e.g., plant growth-promoting bacteria and compost amended) (Ma et al. 2020; Tang et al. 2020a, b; Tu et al. 2020; Xu et al. 2020). Various immobilization mechanisms of Cd^{2+} by biochar in soils were involved, like surface complexation, precipitation, electrostatic attraction, and cation exchange (Xiao et al. 2020). The strong binding of biochar with Cd^{2+} may facilitate the transport of Cd^{2+} by cotransport inducing potential environmental risks. Cao et al. (2021) investigated the cotransport of Cd^{2+} with ball-milled biochar from ramie in terms of different Cd^{2+} and biochar concentrations, and injection sequence. The role of solution chemistry on the cotransport of Cd^{2+} with biochar, such as pH and ionic strength (IS), is still unknown, which might pose a significant effect on their cotransport.

Numerical models are often used to simulate the transport of biochars in quartz sands or natural soils by fitting their breakthrough curves with/without the retention profiles. For the steady-state flow condition, most studies adopted a two-site kinetic model coupled with the advection-dispersion equation, assuming one site was reversible with attachment-detachment and the other was irreversible only with attachment. For example, the two-site kinetic model has been applied for the cotransport modeling of biochar with U(VI) (Sun et al. 2022), humic acid and naphthalene (Yang et al. 2017), iron oxyhydroxide (Wang et al. 2013b), PAHs (Yang et al. 2021), chromate (Jin et al. 2020), sulfamethazine (Yang et al. 2020a), and proteins (Yang et al. 2019). A few studies employed a one-site kinetic model assuming first-order reversible attachment-detachment (e.g., cotransport of biochar with zwitterionic ciprofloxacin (Zhu et al. 2021) or only irreversible attachment (e.g., individual and cotransport of biochar with Cd^{2+}) (Cao et al. 2021; Liu et al. 2021; Wang et al. 2013a). In transient chemical conditions, the release of biochar from the porous media was simulated by assuming equilibrium and kinetic release using the colloid release model during the cotransport with humic acid (Bradford et al. 2015; Wang et al. 2020). Unfortunately, all the above numerical models used for biochar transport only accounted for the attachment/detachment of biochar to/from the solid phase with Langmuir and/or depth-dependent blocking. Many essential processes that pose significant effects either on biochar or contaminants were ignored in the models for simplification, such as the Ostwald ripening of biochar that can be caused by the cations and the presence of mobile and immobile biochar controlling the coexisting contaminant mobility. Therefore, the descriptions of the current numerical models on the biochar individual transport and cotransport with other contaminants were insufficient, incapable of revealing the driving processes that control their mobility.

Despite the comprehensive research on the interactions between Cd^{2+} and biochar, the studies on the cotransport of Cd^{2+} with N-BC are still limited, especially for the unknown influence from the solution chemistry (e.g., pH and IS) and the unclear critical processes driving the mobility of Cd^{2+} and N-BC during the cotransport. Thus, the objectives of our study were to (1) investigate the individual transport behaviors of Cd^{2+} and N-BC under different solution pH and IS, respectively; (2) demonstrate the interactive mechanisms between Cd^{2+} and N-BC and their cotransport behaviors under different solution pH and IS; (3) reveal the underlying key processes controlling the mobility of Cd^{2+} and N-BC during the cotransport with a process-based cotransport numerical model by incorporating the Ostwald ripening of N-BC and the adsorption between Cd^{2+} and mobile/immobile N-BC.

2 Materials and methods

2.1 Preparation of N-BC colloids

Wheat straws sampled from Panzhihua City (China) were carbonized at 500 ℃ for 6 h in an N_2-supported muffle furnace. The produced pristine biochars (P-BCs) were washed with deionized water under an ultrasonication bath and then stood still for 12 h to remove the dissolved impurities in the supernatant. The above cleaning procedure was repeated for 3 times, and then the biochars were dried at 105 ℃. The P-BCs were milled and sieved by a 200-mesh screen for the following dispersion. 15 g P-BCs in 500 ml deionized water were ultrasonicated for 4 h, then centrifugated at 3800 r min^{-1} for 30 min. The supernatants were filtered by 0.45 μm polycarbonate membranes (Whatman, UK) to obtain colloidal solutions with a colloid diameter < 0.45 μm. The colloidal solution was then used as the stock solution. Its concentration was calculated by subtracting the precipitated biochar weighed after drying in the centrifuge tube from 15 g biochar. The obtained nanoscale wheat biochars were labeled as N-BC. The zeta potentials and hydrodynamic diameters of N-BC were determined in KCl solution under different pH (4, 5, 6, and 7) and IS (1, 50, 100, and 150 mM) (Zetasizer Nano ZS, Malvern Panalytical), respectively. The morphology and element analysis of the P-BC and N-BC were conducted using a field emission scanning

electron microscope (FESEM) with energy dispersive X-ray spectroscopy (EDX) (SU8220, HITACHI, Japan) and a transmission electron microscope (TEM) with EDX (Talos F200S G2, Thermo Fisher Scientific).

2.2 Porous medium

0.2–0.5 mm quartz sands (Shengli quartz sand factory, China) were washed with deionized water for 3 times before being soaked with 20% HCl. Afterward, the sands were washed with deionized water and dried at 105 ℃. The quartz sand suspension was prepared using 5 g milled and 200 mesh screened quartz sand with deionized water followed by ultrasonication for 20 min. The supernatant solution containing colloidal quartz sand fraction was then collected and dispersed in KCl solution at different pH (4, 5, 6, and 7) and IS (1, 50, 100, and 150 mM) and used for the zeta potential measurement of quartz sand (Zetasizer Nano ZS, Malvern Panalytical) (Sun et al. 2022).

2.3 Column experiments

Acrylic columns with a height of 12 cm, an inner diameter of 3 cm, and porous mesh screens on both ends were used to wet-pack the quartz sand homogenously. The column bulk density and porosity were adjusted to 1.5 ± 0.1 g cm^{-3} and 0.45 ± 0.02. The columns were initially saturated with KCl solutions for 10 pore volumes (PV) at the designated pH and IS in each scenario with a bottom-up steady-state flow at a Darcy velocity of 0.488 cm min^{-1}. Then 1 mM KBr of 1.5 PVs was injected into each column as a conservative tracer to determine the dispersion coefficient. Ion chromatography was adopted to measure the breakthrough curve (BTC) concentration of Br^- (Metrohm Compact IC 861, Switzerland). For the individual transport experiments, 1.5 PVs of 500 mg L^{-1} N-BC solutions or 10 mg L^{-1} Cd^{2+} solutions were injected, followed by 4 PVs KCl solutions under different pH (4, 5, 6, and 7) and IS (1, 50, 100, and 150 mM), respectively. For the cotransport experiments, 1.5 PVs mixture solutions (500 mg L^{-1} N-BC + 10 mg L^{-1} Cd^{2+}) were also injected in different pH (4, 5, 6, and 7) and IS (1, 50, 100, and 150 mM), respectively. After each column experiment, the quartz sands were collected in 3 layers of each 4 cm into centrifuge tubes to calculate the recovery. 20 mL deionized water was added, followed by an ultrasonic bath for 20 min. The supernatants were collected to determine the retained concentrations of N-BC and Cd^{2+}, respectively. An automatic collector collected the effluents per minute (BS-100 N, Huxi, China). The N-BC concentrations were determined by UV spectrophotometer (UV-2800, Unico Instrument Company, China) at 550 nm. The correlation between absorbance and colloid concentration is shown in Fig. S1. The Cd^{2+} concentrations were determined by ICP-MS (ELAN DRC-e, PerkinElmer, US).

2.4 Numerical modeling

The numerical models of the individual and cotransport of N-BC and Cd^{2+} were set up using the Hydrus-1D code with Phreeqc mode (Jacques et al. 2008). The model domain was composed of 121 nodes with 0.1 cm intervals. The upper and lower boundary conditions were designated as constant pressure heads. For the conservative transport of Br^-, a concentration flux boundary was set as the upper boundary condition where 1 mM Br^- was injected for 1.5 PVs. A zero concentration gradient boundary was assigned for the lower boundary condition. The reactive transport of N-BC and Cd^{2+} applied the same boundary conditions as the conservative transport but with different injected solution concentrations.

2.4.1 Colloid transport modeling

The reactive transport of N-BC was simulated by a first-order kinetic sorption model in a one-dimensional form (Šimůnek et al. 2006):

$$\frac{\partial \theta C_b}{\partial t} + \rho \frac{\partial S_b}{\partial t} = \frac{\partial}{\partial x}\left(\theta D \frac{\partial C_b}{\partial x}\right) - \frac{\partial q C_b}{\partial x} \tag{1}$$

$$\rho \frac{\partial S_b}{\partial t} = \theta \psi_b k_a^b C_b - \rho k_d^b S_b \tag{2}$$

$$\psi_b = 1 - S_b / S_{max}^b \tag{3}$$

where C_b (mol L^{-1}) is the aqueous concentration of N-BC, θ (-) is the volumetric water content, S_b (mol mol^{-1}) is the attached concentration of N-BC on the sand surface, t (min) is time, ρ (g cm^{-3}) is the bulk density, D (cm^2 min^{-1}) is the dispersion coefficient, ψ_b (-) is the blocking function, and q (cm min^{-1}) is the water flux. k_a^b (min^{-1}) and k_d^b (min^{-1}) are the attachment and detachment coefficients for N-BC adsorption to quartz sand, respectively. S_{max}^b (mol mol^{-1}) is the maximum attainable N-BC concentration on the sand surface.

2.4.2 Cd^{2+} transport modeling

The reactive transport of Cd^{2+} was simulated based on the modified one-dimension advection-dispersion equation with first-order kinetic sorption (Šimůnek et al. 2006):

$$\frac{\partial \theta C_c}{\partial t} + \rho \frac{\partial S_c}{\partial t} = \frac{\partial}{\partial x}\left(\theta D \frac{\partial C_c}{\partial x}\right) - \frac{\partial q C_c}{\partial x} \tag{4}$$

$$\rho \frac{\partial S_c}{\partial t} = \theta \psi_c k_a^c C_c - \rho k_d^c S_c \quad (5)$$

$$\psi_c = 1 - S_c / S_{max}^c \quad (6)$$

where C_c (mol L^{-1}) is the aqueous concentration of Cd^{2+}, S_c (mol mol^{-1}) is the attached concentration of Cd^{2+} on the sand surface, ψ_c (-) is the blocking function, k_a^c (min^{-1}) and k_d^c (min^{-1}) are the attachment and detachment coefficients for Cd^{2+} adsorption to quartz sand, respectively. S_{max}^c (mol mol^{-1}) is the maximum attainable Cd^{2+} concentration on the sand surface.

2.4.3 Cotransport modeling

The cotransport modeling of N-BC with Cd^{2+} was also based on the modified advection-dispersion equations. A ripening term was added into Eq. (2) to fit the potential ripening BTCs of N-BC in the presence of Cd^{2+} (Wang et al. 2015):

$$\rho \frac{\partial S_b}{\partial t} = \theta \psi_b k_a^b C_b - \rho k_d^b S_b + \theta S_b C_b k_{rip} \quad (7)$$

where k_{rip} (min^{-1}) is the ripening coefficient accounting for the enhanced particle deposition on the sand surface due to the attractive particle-particle interaction.

The mass balance equation for Cd^{2+} was given by (Šimůnek et al. 2006):

$$\frac{\partial \theta C_c}{\partial t} + \rho \frac{\partial S_c}{\partial t} + \frac{\partial \theta C_b S_c^m}{\partial t} + \rho \frac{\partial S_b S_c^{im}}{\partial t} = \frac{\partial}{\partial x}\left(\theta D \frac{\partial C_c}{\partial x}\right) - \frac{\partial q C_c}{\partial x} + \frac{\partial}{\partial x}\left(\theta D \frac{\partial C_b S_c^m}{\partial x}\right) - \frac{\partial q C_b S_c^m}{\partial x} \quad (8)$$

$$\frac{\partial \theta C_b S_c^m}{\partial t} = \frac{\partial}{\partial x}\left(\theta D \frac{\partial C_b S_c^m}{\partial x}\right) - \frac{\partial q C_b S_c^m}{\partial x} + \theta \psi^m k_a^m C_b - \theta k_d^m C_b S_c^m \quad (9)$$

$$\rho \frac{\partial S_b S_c^{im}}{\partial t} = \theta \psi^{im} k_a^{im} C_b - \rho k_d^{im} S_b S_c^{im} \quad (10)$$

$$\psi^m = C_b / C_b^{ref} \quad (11)$$

$$\psi^{im} = S_b / S_b^{ref} \quad (12)$$

where S_c^m (mol mol^{-1}) and S_c^{im} (mol mol^{-1}) are the adsorbed Cd^{2+} concentration on the mobile and immobile N-BC, respectively. ψ^m (-) and ψ^{im} (-) adjust the sorption rate of Cd^{2+} to the present mobile and immobile N-BC, respectively. k_a^m (min^{-1}) and k_d^m (min^{-1}) are the attachment and detachment coefficients of Cd^{2+} to the mobile N-BC, while k_a^{im} (min^{-1}) and k_d^{im} (min^{-1}) are the attachment and detachment coefficients of Cd^{2+} to the immobile N-BC, respectively. C_b^{ref} (mol L^{-1}) and S_b^{ref} (mol mol^{-1}) were the reference concentrations of mobile and immobile N-BC for which the attachment rates were valid, respectively.

2.4.4 Model calibration

The dispersion coefficient (D) was assigned as the same value for each model, which was estimated by inversing the BTCs of Br^-. The reactive transport parameters related to the N-BC transport (k_a^b, k_d^b, and S_{max}^b), Cd^{2+} transport (k_a^c, k_d^c, and S_{max}^c), and cotransport (k_a^b, k_d^b, S_{max}^b and k_{rip} of N-BC; k_a^c, k_d^c, S_{max}^c, k_a^m, k_d^m, k_a^{im}, k_d^{im}, C_b^{ref}, and S_b^{ref} of Cd^{2+}), were estimated by their BTCs using PEST with the Marquardt-Levenberg method (Doherty 2015). The composite parameter sensitivity of each model under different scenarios was also calculated by PEST with the following relation (Doherty 2015):

$$csp_i = \frac{\left[\mathbf{J}^t \mathbf{Q} \mathbf{J}\right]_{ii}^{1/2}}{n} \quad (13)$$

where csp_i was the composite sensitivity of parameter i. $\mathbf{J}$, $\mathbf{Q}$, and n were the Jacobian matrix, weight matrix, and observation numbers of non-zero weights. The parameter sensitivity analysis can reveal the dominant process by evaluating how the model responded to the parameter change. The Derjaguin–Landau–Verwey–Overbeek (DLVO) theory and isothermal adsorption models (i.e., Freundlich, Langmuir, and Temkin models) were are employed to investigate the interaction of N-BC with quartz sand and Cd^{2+} with N-BC, respectively (Text S1 and S2).

3 Results and discussion

3.1 Characteristics of N-BC

Figure 1a and c show that the milling treatment produced more nanoparticles in N-BC than P-BC (Fig. 1a and c). The diameter of the single N-BC nanoparticle was 22.21 ± 13.22 nm that was calculated based on the TEM image (Fig. S2). The elemental composition of the N-BC was C (70.86%), O (17.93%), Si (5.53%), K (3.4%), Ca (0.77%), Mg (0.34%), P (0.15%) and Al (0.12%), which did not show significant difference from P-BC (Fig. 1b and d). FTIR results revealed that the oxygen-containing functional groups, i.e., -OH, C=O, COO^-, and C-O, increased after grinding (Fig. S3) (Balaz 2018; Cao et al. 2021). The average pore size, pore volume, and specific surface area also increased (Table S1).

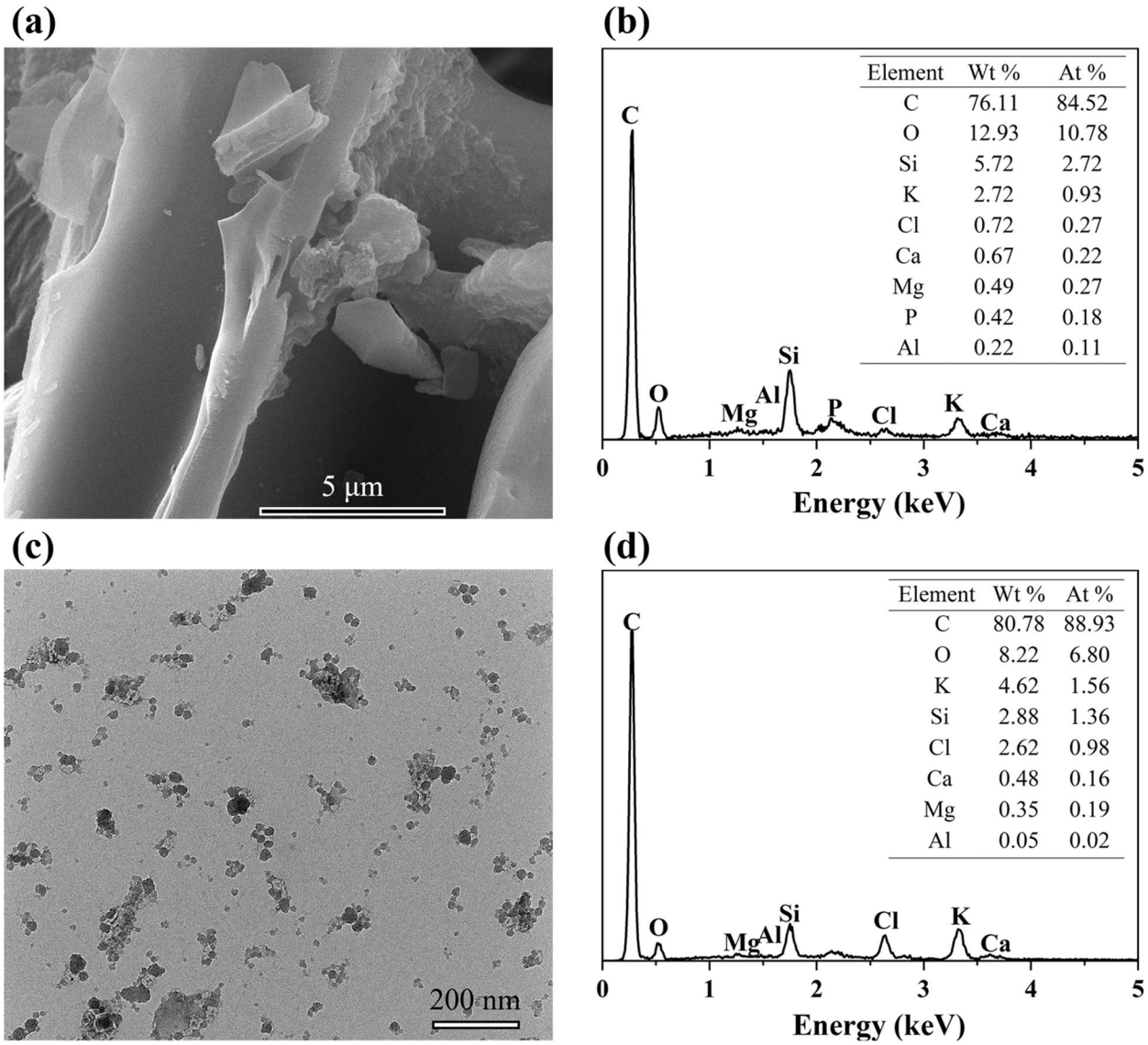

Fig. 1 The FESEM and EDX images of P-BC (**a**, **b**), and the TEM and EDX images of N-BC (**c**, **d**), respectively

The varying hydrodynamic diameters of N-BC in different concentrations with time are presented in Fig. S4. The insignificant fluctuation of hydrodynamic diameter indicated good colloid stability of N-BC. The average hydrodynamic diameters of 200 and 500 mg L^{-1} N-BC solutions were 226.2 nm and 215.3 nm, respectively. The zeta potentials of N-BC and quartz sand decreased with the decrease in IS or increase in pH (Table S2). The hydrodynamic diameters of N-BC varied little at different pH around 250 nm, but increased with IS from 228 nm at 1 mM to 1107 nm at 150 mM due to the compressed double-layer leading to colloid aggregation. Fig. S5 shows that the Langmuir model fitted the isothermal adsorption experiments well with an R^2 of 0.975 and 112 mg g^{-1} maximum adsorption capacity (Table S3), indicating the adsorption mode of Cd^{2+} on N-BC was a reversible adsorption process with limited adsorption sites.

3.2 Individual transport of N-BC

The transport of N-BC was retarded by the quartz sand as compared to the conservative transport of Br^-, and was decreased with the increasing solution IS (Fig. 2a). The maximum C/C_0 of N-BC was reduced from 0.85 at 1 mM to 0.4 at 150 mM, and the recovery rate of the effluent N-BC was also reduced from 96.2% at 1 mM to 37.1% at 150 mM (Table S4). The retarded transport of N-BC with increasing IS was attributed to the elevated

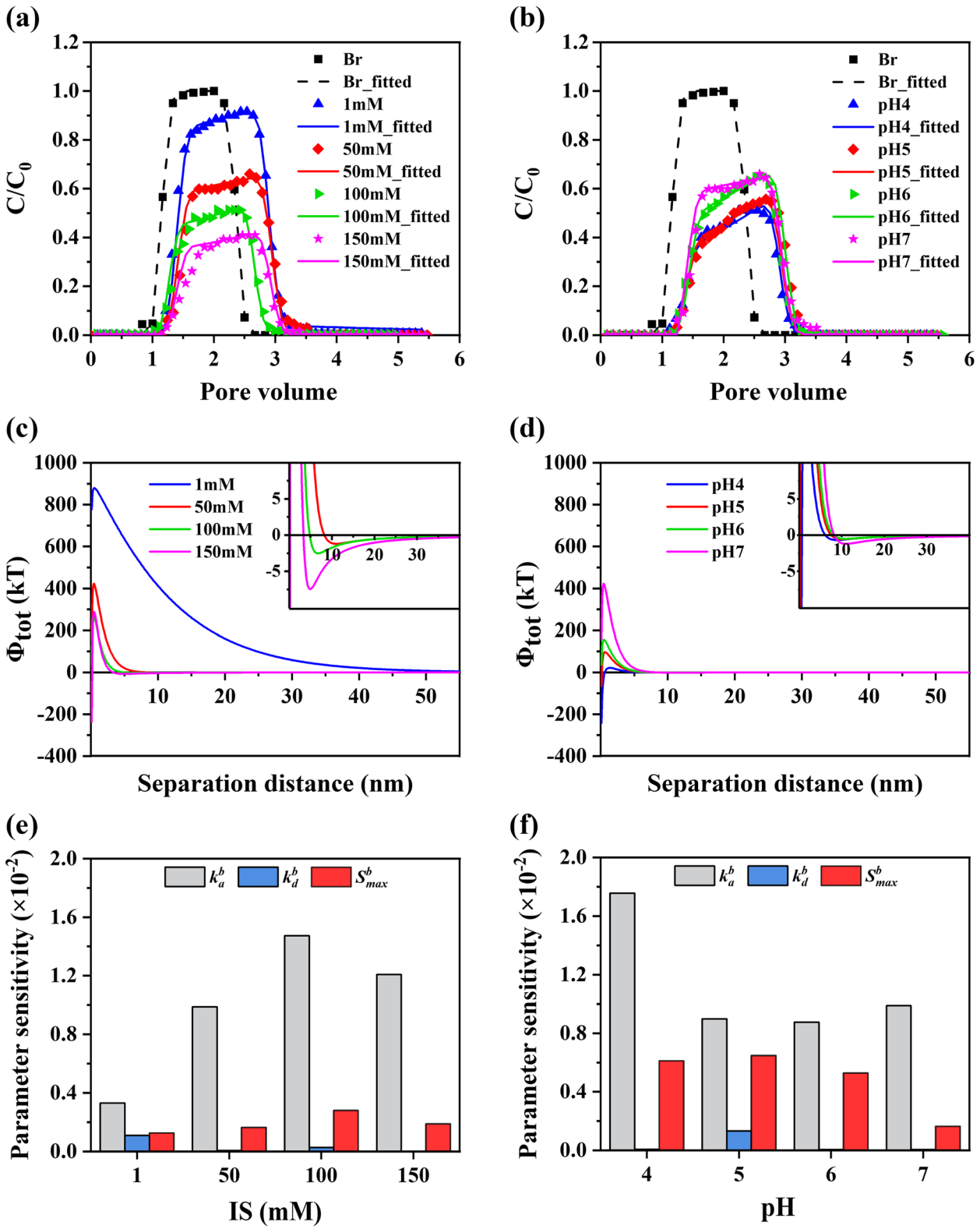

Fig. 2 **a**, **b** The measured and fitted BTCs of N-BC. **c**, **d** The calculated total interaction energy curves. **e**, **f** The calculated parameter sensitivities. **a**, **c**, **e** are at different IS under pH 7, and **b**, **d**, **f** are at different pH under 50 mM IS

electrostatic attraction indicated by the increased zeta potentials of N-BC and quartz sand (Table S2), which promoted the deposition of N-BC on the sand surface. As illustrated in Fig. 2c and Table S4, the calculated maximum energy barrier (Φ_{max}) was as high as 879.67 kT (i.e., k is Boltzmann constant and T is absolute temperature) at 1 mM but reduced 3 times to 287.92 kT at 150 mM. On the contrary, the secondary minimum (Φ_{sec}) decreased from −0.005 kT at 1 mM to -7.45 kT at 150 mM, which might promote the deposition of N-BC at the secondary minimum. The model results well fitted the observed data with $R^2 > 0.96$, indicating that the first-order kinetic sorption assumption was valid for N-BC transport without considering the straining process (Table S4). The model-fitted k_a^b was observed to increase with IS but k_d^b decreased, which means the attachment process became increasingly faster while the detachment became slower as IS increased. Meanwhile, S_{max}^b also increased with IS providing more sorption sites. Positive values of Φ_{pri} were observed at 1, 50, and 100 mM IS, suggesting that the deposition at the primary minimum was impossible due to the electrostatic repulsive force. The attachment of N-BC on the sand surface was via the deposition at the secondary minimum, which could be reversible since the absolute value of Φ_{sec} was comparable to 1.5 kT (i.e., the average Brownian diffusion thermal energy) (Shen et al. 2007). At 150 mM IS, although Φ_{pri} was reduced to -237.85 kT, it was still unlikely for N-BC to deposit at the primary minimum due to the high primary energy barrier. The main process was still the attachment at the secondary minimum since Φ_{sec} was reduced to -7.45 kT. The parameter sensitivity analysis showed that the transport of N-BC was very sensitive to k_a^b in all conditions, indicating that attachment was the dominant process (Fig. 2e).

Figure 2b shows that the mobility of N-BC was enhanced with the increase in pH. The recovery rate of the effluent N-BC was increased from 53.0% at pH 4 to 63.7% at pH 7 (Table S4). The increase of pH promoted the transport of N-BC due to the elevated electrostatic repulsive force proved by the decreased zeta potentials (Table S2). Based on the DLVO calculations, Φ_{max} was enhanced significantly as pH increased (Fig. 2d), hampering the deposition at the primary minimum. Although negative values of Φ_{pri} were observed at pH 4 and 5, only Φ_{max} at pH 4 was less than 25 kT which was the threshold for colloid stability (Tadros 2014), indicating the possibility of deposition at the primary minimum at pH 4. The deposition at pH 5, 6, and 7 at the primary minimum was non-existent. The absolute values of Φ_{sec} were all less than 1.5 kT (the Brownian diffusion thermal energy), resulting in a weak deposition at the secondary minimum. Thus, the retardation at pH 4 was attributed to the deposition both at the primary and secondary minimum, while the retardation at pH 5, 6, and 7 resulted from the deposition at the secondary minimum. Figure 2f shows that the transport of N-BC was still very sensitive to k_a^b while the influence of S_{max}^b was nonnegligible under acid conditions. It means that the variation of sorption sites induced by the pH change can significantly impact the transport of N-BC in porous media.

3.3 Individual transport of Cd^{2+}

Figure 3a shows the measured and simulated individual transport of Cd^{2+} under different IS. At 1 mM, the BTC started to elute at 1.4 PVs and reached a peak of 0.85. While at 150 mM, the elution time advanced to 1.2 PV and reached a peak of 0.95. The effluent recovery rate increased from 73.1% at 1 mM to 96.7% at 150 mM (Table S5), demonstrating the facilitating role of increasing IS on Cd^{2+} mobility. The Cd^{2+} transport model with an assumption of first-order kinetic sorption showed an excellent description of the observed BTC data with $R^2 > 0.93$. k_a^c decreased from 1.77×10^{-1} to 3.90×10^{-3} min^{-1}, k_d^c increased from 4.09×10^{-5} to 1.03×10^{-4} min^{-1}, and S_{max}^c decreased from 3.22×10^{-9} to 2.85×10^{-9} mol mol^{-1} as IS increased from 1 to 150 mM. The model parameter sensitivity analysis revealed that the model responses to k_a^c, k_d^c, and S_{max}^c were very sensitive at 1 mM, but the sensitivity dramatically decreased as IS increased (Fig. 3c). All the above results demonstrated that the sorption process weakened as IS increased, suggesting the promoted effect of IS on Cd^{2+} transport. The enhanced mobility of Cd^{2+} was due to the increased competition with the coexisting K^+ at high IS and the increased zeta potential of quartz sand enhancing the electrostatic repulsive force with Cd^{2+} (Table S2) (Park et al. 2017).

Figure 3b shows the measured and simulated individual transport of Cd^{2+} under different pH. The BTCs under pH 4, 5, and 6 almost started to elute at the same time from 1.2 PVs. The BTC under pH 7 eluted from 1.4 PVs. The effluent recovery rate decreased from 99.1% at pH 4 to 89.4% at pH 7. The BTC data was well fitted with $R^2 > 0.95$. The calibrated k_a^c, k_d^c, and S_{max}^c were all increased from 2.93×10^{-3} min^{-1}, 1.06×10^{-6} min^{-1}, and 6.65×10^{-12} mol mol^{-1} at pH 4 to 1.54×10^{-2} min^{-1}, 5.94×10^{-5} min^{-1}, and 3.14×10^{-9} mol mol^{-1} at pH 7, respectively (Table S5). The attachment of Cd^{2+} to quartz sand was still the dominant process, and its influence on the model results also increased with pH (Fig. 3d). All these results revealed the retardation of Cd^{2+} by the increasing pH. This retardation was attributed to (1) the enhanced electrostatic attraction force with the increase of pH indicated by the zeta potentials (Table S2); (2) less

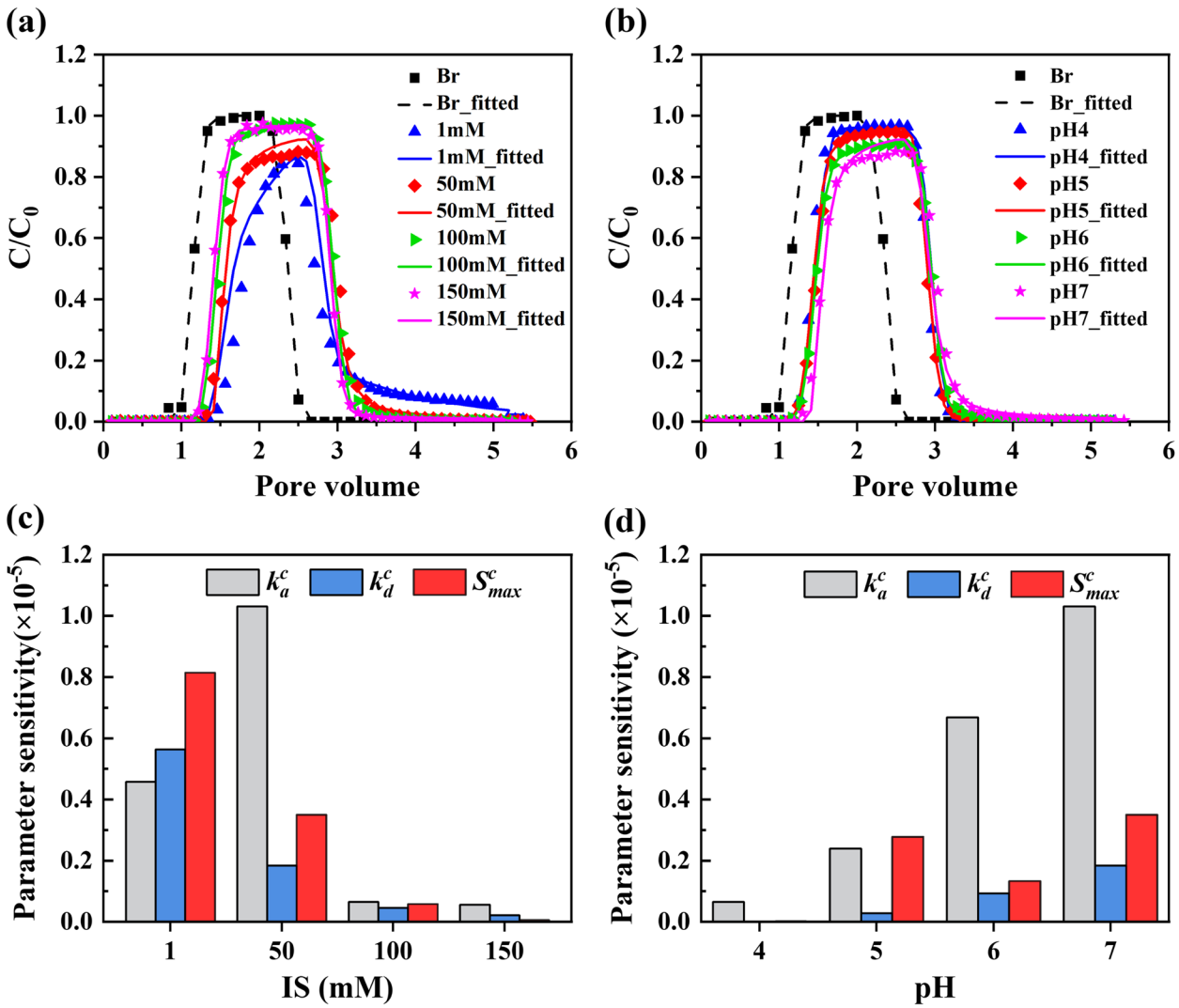

Fig. 3 **a**, **b** The breakthrough and fitting curves of Cd^{2+}. **c**, **d** The calculated parameter sensitivities. **a**, **c** are at different IS under pH 7, and **b**, **d** are at different pH under 50 mM IS

H^+ to compete with Cd^{2+} for the sorption sites leading to more retained Cd^{2+} in the column.

3.4 Effect of solution IS on the cotransport

The cotransport BTCs of N-BC with Cd^{2+} under different solution IS are illustrated in Fig. 4. The mobility of N-BC in the presence of Cd^{2+} was decreased by the increase of IS with effluent recovery reduced from 94.7% at 1 mM to 7.7% at 150 mM (Table 1). These effluent recoveries of N-BC in the cotransport scenarios were less than those in the individual transport, indicating the retardation effect of Cd^{2+} on N-BC mobility. It might be due to the previously attached Cd^{2+} on the quartz sand providing positively-charged favorable sorption sites for the negatively-charged N-BC and facilitating the deposition of N-BC on the sand surface. This can be proved by the enhanced S^b_{max} of N-BC in the cotransport models, which were all greater than those in the individual transport experiments (Table 1). Fig. S6a shows that the adsorption capacity of N-BC for Cd^{2+} decreased with the increase of IS due to the ion competition, which might promote N-BC retention in low IS by forming cation bridges between N-BC and quartz sand. However, the retained recovery of N-BC in the cotransport at 1 mM IS only increased by 3% from 1.9% to 4.9% compared to its individual transport, less than that at 150 mM IS increased by 27.6% from 56% to 83.6%. These results indicated that the interaction between quartz sand and N-BC was still the dominant process, while the Cd^{2+}-induced N-BC retention became significant as the IS increased. The decline

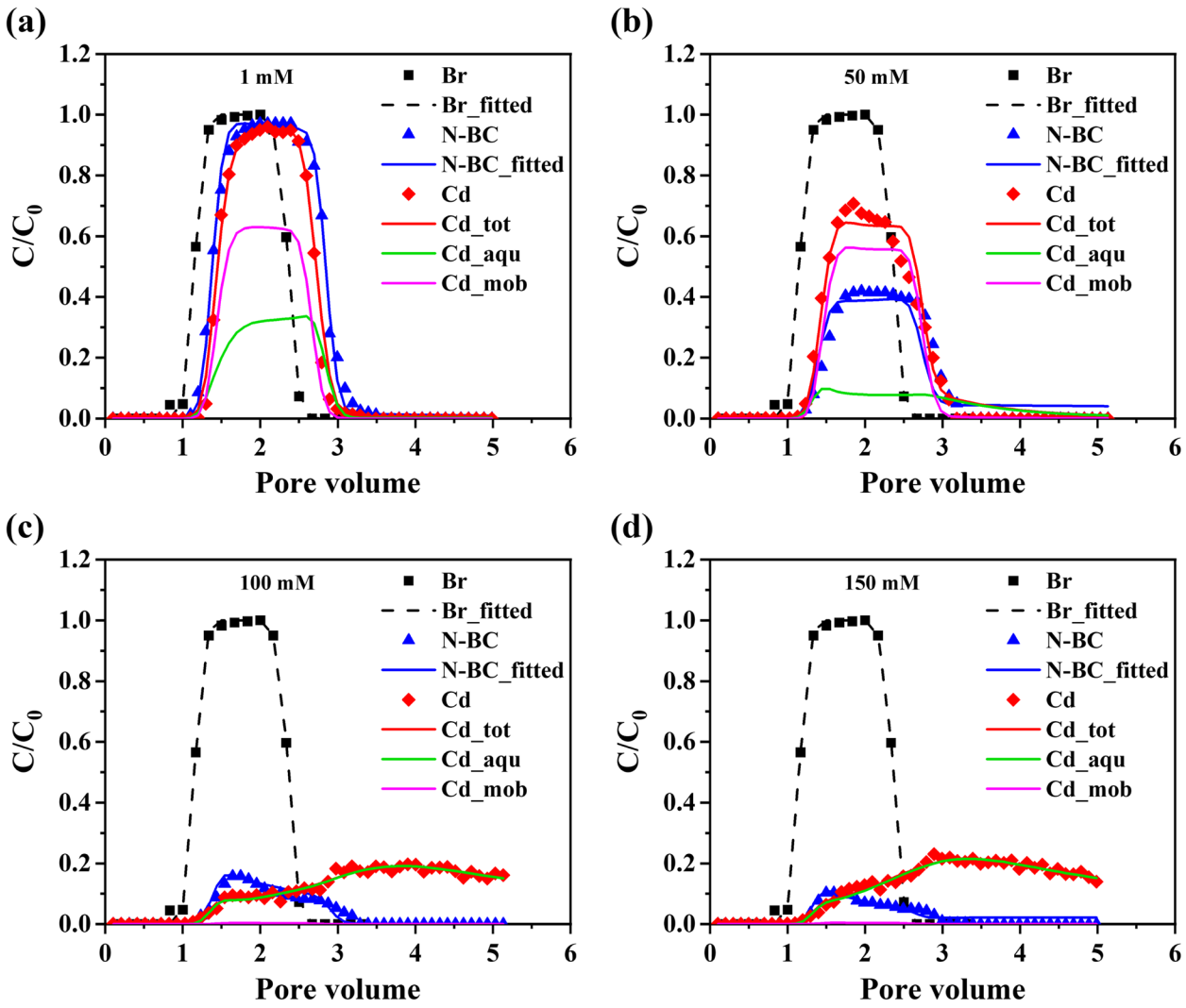

Fig. 4 The cotransport breakthrough curves and fitting curves of Cd^{2+} and N-BC at different IS under pH 7. The total Cd^{2+} concentration (Cd_tot) was the sum of the aqueous free Cd^{2+} (Cd_aqu) and the Cd^{2+} adsorbed on the mobile N-BC (Cd_mob) in the effluent

Table 1 The cotransport fitting parameters and recovery of N-BC at different IS and pH

IS (mM)	pH	k_a^b (min^{-1})	k_d^b (min^{-1})	S_{max}^b (mol mol^{-1})	k_{rip} (min^{-1})	R^2	Experimental Recovery (%)		
							Effluent	Retained	Total
1	7	1.59×10^{-3}	8.15×10^{-5}	3.78×10^{-4}	2.13	0.996	94.7	4.9	99.7
50	7	7.02×10^{-2}	2.50×10^{-5}	1.46×10^{-4}	3.18	0.920	50.7	44.0	94.6
100	7	1.27×10^{-1}	9.90×10^{-7}	1.52×10^{-5}	6.64	0.946	17.3	72.2	89.5
150	7	1.59×10^{-1}	6.29×10^{-7}	1.49×10^{-5}	7.03	0.816	7.7	83.6	91.3
50	4	1.37×10^{-1}	1.36×10^{-5}	3.46×10^{-5}	5.72	0.917	18.5	79.5	98.0
50	5	1.35×10^{-1}	1.36×10^{-5}	3.82×10^{-5}	5.56	0.917	20.6	76.4	97.0
50	6	5.68×10^{-2}	1.62×10^{-5}	2.78×10^{-5}	5.12	0.970	45.8	50.2	96.0

of C/C_0 at the plateau of the BTCs was observed in the BTCs at 100 and 150 mM, where C/C_0 decreased with PV after the first BTC peak at 1.6 and 1.5 PV (Fig. 4c and d). This phenomenon did not exist in the individual transport scenarios under all conditions but existed in the cotransport due to (1) the deposition of N-BC on the previously attached N-BC on the sand surface, namely Ostwald ripening, promoted by the cation bridging of Cd^{2+}; (2) the straining of greater aqueous N-BC homo-aggregates in the pores induced by aggregation, which can be more significant as the pores became more plugged; (3) the compressed double layer of N-BC in the high IS at 100 and 150 mM facilitating the above two processes. Both aggregation and ripening might be occurring simultaneously, however, it was not possible to separate these effects from the collected data (Liang et al. 2019; Xu et al. 2021). Therefore, this phenomenon induced by aggregation and/or ripening was all referred to as ripening in the following text for simplification. The simulated retention profiles of N-BC also showed that the retention at the column inlet of N-BC at 100 and 150 mM was 2 to 3 times higher than at 1 and 50 mM IS due to the ripening of N-BC at the inlet (Fig. 5a). This process posed a significant influence on N-BC transport as illustrated by the parameter sensitivity that the model response to k_{rip} was after k_a^b (Fig. S7a). It is worth mentioning that the ripening was highly related to the colloidal property. It can be observed at 100 mM IS in a ramie-derived ball-milled biochar transport but without Cd^{2+}, of which particle size was 1167 nm at 100 mM larger than 589 nm of this study (Cao et al. 2021). The preparation and characteristics of nanoscale biochar determined the particle size under different solution chemistry.

The experimental BTCs of Cd^{2+} in the presence of N-BC at different IS were distinct from the Cd^{2+} individual transport scenarios (Fig. 4). The experimental effluent recoveries decreased with the increase of IS from 78.14% at 1mM to 35.91% at 150 mM in the presence of N-BC (Table 2), which were contrary to the Cd^{2+} individual transport that the effluent recoveries increased with IS. It was observed that the experimental effluent Cd^{2+} concentrations were positively correlated with the effluent N-BC. The adsorption of Cd^{2+} on the immobile N-BC significantly reduced Cd^{2+} mobility. It is worth mentioning that both the effluent recoveries of N-BC and Cd^{2+} decreased in the cotransport compared to their individual transport, except that the effluent recovery of Cd^{2+} increased in the cotransport at 1 mM IS and pH 7 compared to its individual transport. In the former case, the co-presence of N-BC and Cd^{2+} promoted the retention of each other in the column. The potential effect of their competition for the adsorption sites on the sand surface was insignificant. In the latter case, the increased mobility of Cd^{2+} at 1 mM IS and pH 7 in the presence of N-BC could be due to the high adsorption capacity of N-BC for Cd^{2+} carrying Cd^{2+} for cotransport (Fig. S6a) and/or the competition of N-BC with Cd^{2+} for the adsorption sites on the sand surface, promoting the transport of Cd^{2+}. The BTCs of Cd^{2+} at 100 and 150 mM IS displayed long tails compared to those at 1 and 50 mM, indicating the release of retained Cd^{2+} from the columns was due to the increased competition with the coexisting K^+ at high IS.

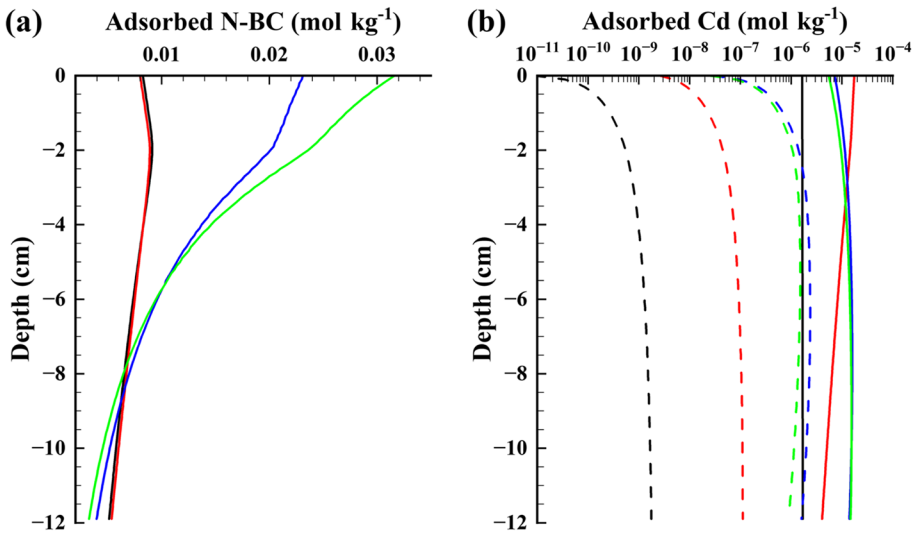

Fig. 5 The simulated vertical profiles of **a** the immobile N-BC on sand surface and **b** retained Cd^{2+} on the sand surface (solid line) and on the immobile N-BC (dashed line) at 1 mM (black), 50 mM (red), 100 mM (blue), and 150 mM (green) IS, respectively

Table 2 The experimental and model recoveries of Cd^{2+} in the cotransport experiments

IS (mM)	pH	Experimental Recovery (%)			Model Recovery (%)					
		Effluent	Retained	Total	Effluent		Retained			Total
					In aqueous phase	On mobile N-BC	On quartz sand	On immobile N-BC	In aqueous phase	
1	7	78.14	20.71	98.85	35.66	59.1	5.23	0.01	0	100
50	7	56.39	38.79	95.18	15.21	54.86	29.42	0.26	0.25	100
100	7	37.55	57.74	95.29	40.9	0.36	44.06	5.85	8.83	100
150	7	35.91	63.11	99.02	46.63	0.32	40.86	3.73	8.46	100
50	4	52.95	44.59	97.54	84.13	14.58	0.45	0.16	0.68	100
50	5	44.51	51.08	95.59	46.29	15.39	33.64	1.87	2.81	100
50	6	43.47	55.47	98.94	28.26	28.09	36.95	1.7	5	100

The cotransport models fitted the transport of Cd^{2+} well by considering the interactions of Cd^{2+} with N-BC and quartz sand in the columns (Fig. 4). Besides the simulated total effluent Cd^{2+} concentrations, the cotransport models also presented the concentrations of aqueous free Cd^{2+} and the Cd^{2+} adsorbed on the mobile N-BC in the effluents. The results showed that 59.1% and 54.86% of the total Cd concentrations adsorbed on the mobile N-BC in the effluents at 1 and 50 mM IS, respectively, which eluted along with 94.7% and 50.7% effluent N-BC (Tables 1 and 2). And the adsorbed Cd^{2+} on the mobile N-BC decreased to 0.36% and 0.32% along with the decrease of effluent N-BC to 17.3% and 7.7% at 100 and 150 mM IS, respectively (Fig. 4c and d). The distinct positive correlation of the adsorbed Cd^{2+} on the mobile N-BC with the effluent N-BC revealed the significant cotransport of N-BC with Cd^{2+} and high affinity of Cd^{2+} to N-BC at high IS (i.e., 100 and 150 mM). Figure 4c and d display long tails of the Cd^{2+} BTCs which were mainly the aqueous Cd^{2+} with 40.9% and 46.63% of the total Cd^{2+} concentration at 100 and 150 mM IS revealed by the cotransport models, respectively. The Cd^{2+} adsorbed on the mobile N-BC was only 0.36% and 0.32%, respectively (Table 2). The tails started from 3 PVs which corresponded to the effluent time of the background KCl solution. These results suggested that the Cd^{2+} in the long tails was in the form of aqueous Cd^{2+} and might originate from the desorption of the Cd^{2+} adsorbed on the immobile N-BC which remained only 5.85% and 3.73% at 100 and 150 mM IS in the columns after the experiments. The simulated vertical profiles revealed that the retained Cd^{2+} concentrations on the immobile N-BC were all lower than those on the sand surface under all conditions (Fig. 5b). The Cd^{2+} concentrations on the immobile N-BC increased with the column depth, contrary to the decrease of adsorbed N-BC with depth, demonstrating the release of Cd^{2+} from the immobile N-BC eluted by the background solution. The parameter sensitivity analysis illustrated that the responses of the cotransport model to the parameters followed the sequence of the parameters related to immobile N-BC (k_a^{im}, k_d^{im}, S_b^{ref}) > quartz sand (k_a^c, k_d^c, S_{max}^c) > mobile N-BC (k_a^m, k_d^m, C_b^{ref}) (Fig. S7b). These results indicated that the dominant process was the interaction of Cd^{2+} with the immobile N-BC driving Cd^{2+} transport. The Cd^{2+} adsorption on and desorption from the immobile N-BC controlled the retention and release of Cd^{2+} during the cotransport scenarios. It is worth mentioning that the desorption of Cd^{2+} from the mobile N-BC was negligible since the parameter sensitivities of k_d^m were zero under all conditions, and the calibration of k_d^m showed very low confidence.

3.5 Effect of solution pH on the cotransport

The cotransport BTCs of N-BC with Cd^{2+} under different solution pH are illustrated in Fig. 6. The retained N-BC decreased from 79.5% at pH 4 to 44.0% at pH 7 (Table 1), which was due to enhanced electrostatic repulsive force via the expansion of the electrical double layer indicated by the decreased zeta potentials (Table S2). The retained concentrations of N-BC in the presence of Cd^{2+} were all greater than those in the absence of Cd^{2+} at different pH, suggesting the retardation of Cd^{2+} on N-BC transport. Fig. S6b shows that the adsorption capacity of N-BC for Cd^{2+} increased with the increase of pH due to the enhanced negatively charged N-BC (Table S2). However, the retained N-BC recovery in the cotransport at pH 4 increased by 37.3% from 42.2% to 79.5% compared to its individual transport, higher than that at pH 7 only increased by 13.1% from 30.9% to 44%. These results demonstrated that the Cd^{2+}-induced N-BC

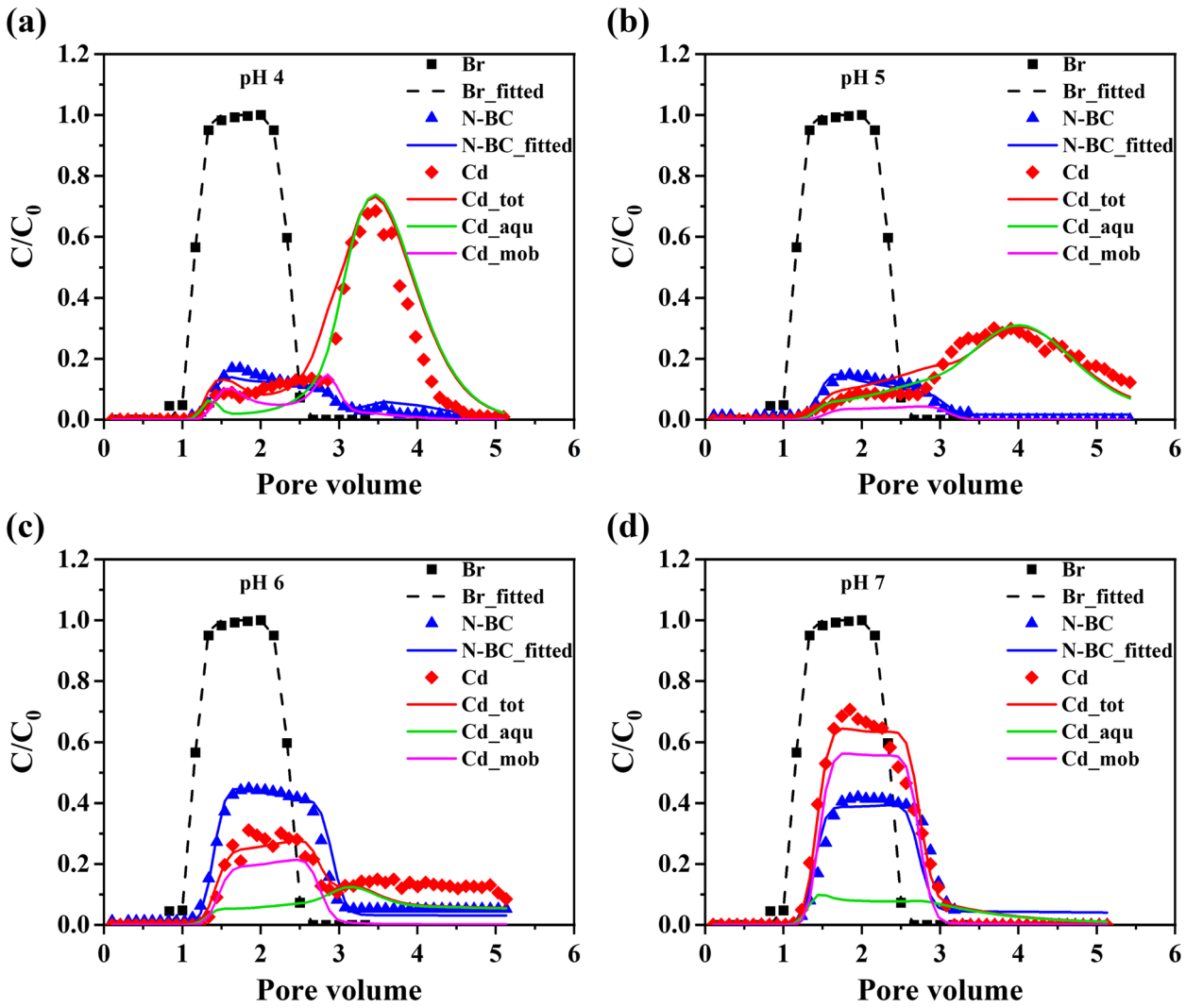

Fig. 6 The cotransport breakthrough curves and fitting curves of Cd^{2+} and N-BC at different pH under 50 mM IS. The total Cd^{2+} concentration (Cd_tot) was the sum of the aqueous free Cd^{2+} (Cd_aqu) and the Cd^{2+} adsorbed on the mobile N-BC (Cd_mob) in the effluent

retention was significant in low pH, while the interaction between N-BC and quartz sand became dominant as pH increased. The ripening phenomena were observed under all conditions and were more significant at lower pH. It can be proved by the simulated vertical profiles that the deposited N-BC concentrations decreased with column depth and the increase of pH (Fig. 7a). Large amounts of N-BC were retained in the upper layers at pH 4 and 5 due to the enhanced van der Waals attractive force between N-BC and quartz sand in acid pH indicated by the increased zeta potentials (Table S2), resulting in the significant ripening effect. The parameter sensitivity analysis demonstrated that the adsorption to the quartz sand surface was still the main process that controlled N-BC transport and the ripening effect was nonnegligible (Fig. S8a). The calibrated transport parameters showed that k_a^b and S_{max}^b were all increased in the presence of Cd^{2+}, indicating that the adsorbed Cd^{2+} on the quartz sand provided additional sorption sites and enhanced the adsorption rate of N-BC (Table 1).

The transport of Cd^{2+} in the presence of N-BC showed divergent BTCs compared to the absence of N-BC (Fig. 6). The experimental recoveries of the effluent Cd^{2+} decreased from 52.95% at pH 4 to 43.47% at pH 6, and then increased to 56.39% at pH 7 (Table 2). It was observed that the BTCs of Cd^{2+} before 2.8 PVs gradually increased with the effluent N-BC concentrations as pH increased from 4 to 7. A positive correlation between the BTCs of Cd^{2+} before 2.8 PVs and the BTCs of N-BC can be deduced, indicating a cotransport of Cd^{2+} with N-BC promoting the mobility of Cd^{2+}.

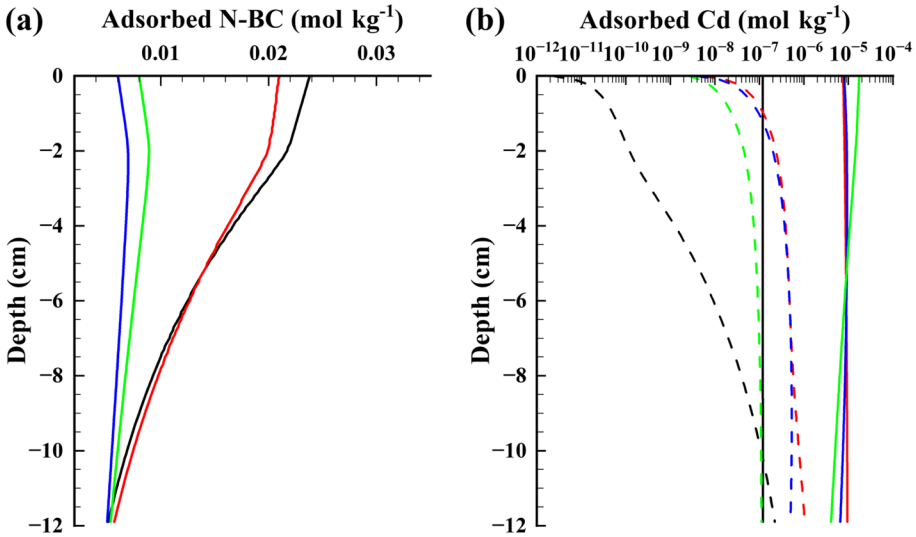

Fig. 7 The simulated vertical profiles of **a** the immobile N-BC on sand surface and **b** retained Cd^{2+} on the sand surface (solid line) and on the immobile N-BC (dashed line) at pH 4 (black), pH 5 (red), pH 6 (blue), and pH 7 (green), respectively

After 2.8 PVs, a high BTC peak of Cd^{2+} was observed at pH 4, which gradually decreased with the increase of pH. These phenomena can be attributed to the reduced competition of H^+ with Cd^{2+} and the increased electrostatic attraction between the immobile N-BC and Cd^{2+} indicated by the decreasing zeta potential of N-BC (Fig. S6b and Table S2). This trend was consistent with the individual transport of Cd^{2+} that the BTCs of Cd^{2+} decreased with the increasing pH (Fig. 3b).

The BTCs of Cd^{2+} in the presence of N-BC were simulated well at different pH (Fig. 6). The model results revealed that the simulated BTCs of Cd^{2+} adsorbed on the mobile N-BC (i.e., the purple curves) were positively correlated to the BTCs of N-BC that were increased with pH. The effluent Cd^{2+} concentrations in the BTCs after 2.8 PVs (i.e., the blue curves) were mainly from the desorption of Cd^{2+} adsorbed on the immobile N-BC. It can be proved by the simulated vertical profiles that the retained Cd^{2+} concentrations on the immobile N-BC increased with pH but were still less than those on the sand surface (Fig. 7b; Table 2). The parameter sensitivity analysis revealed that the responses of the cotransport models to the parameters followed the sequence of the parameters related to immobile N-BC (k_a^{im}, k_d^{im}, S_b^{ref}) > quartz sand (k_a^c, k_d^c, S_{max}^c) > mobile N-BC (k_a^m, k_d^m, C_b^{ref}) (Fig. S8b). The low parameter sensitives of k_a^m, k_d^m, and C_b^{ref} indicated that the interaction of Cd^{2+} with mobile N-BC played a minor role. These results suggested that the driving process controlling Cd^{2+} transport at different pH was the interaction of Cd^{2+} with immobile N-BC. Despite the high affinity of Cd^{2+} with N-BC, the adsorption of Cd^{2+} to the immobile N-BC posed a more significant effect on Cd^{2+} transport than the adsorption to the mobile N-BC, which was due to the retardation effect of the immobile N-BC on Cd^{2+} transport.

4 Conclusion

This study demonstrated variable transport behaviors of Cd^{2+} and N-BC during their individual and cotransport scenarios under different pH and IS, which indicated the significant effects of solution chemistry on their transport patterns. For the individual transport scenarios, increasing IS and decreasing pH retarded the transport of N-BC but promoted the transport of Cd^{2+}. For the cotransport scenarios, the presence of Cd^{2+} promoted the deposition of N-BC on the quartz sand surface with increasing IS and decreasing pH by providing additional sorption sites and led to the ripening of N-BC via cation bridging. In general, the presence of N-BC retarded the transport of Cd^{2+} under all conditions. However, lower pH and higher IS could facilitate the release of Cd^{2+} from the immobile N-BC. The process-based cotransport model with parameter sensitivity analysis revealed that the Cd^{2+} adsorption on and desorption from the immobile N-BC controlled the retention and release of Cd^{2+} at variable pH and IS, while the influence of mobile N-BC on Cd^{2+} transport was minor. Our findings demonstrated that despite the retardation effect of N-BC on the Cd^{2+} mobility, groundwater's transient solution chemistry conditions could still lead to the release of Cd^{2+} from the immobile N-BC. It is worth mentioning that this study did not consider the

influence of coexistent natural substances, such as multivalent ions, dissolved organic matters, and soil colloids. They may pose distinct impacts on the co-migration of Cd^{2+} with N-BC that need further investigations.

Supplementary Information

The online version contains supplementary material available at https://doi.org/10.1007/s42773-023-00211-3.

Additional file 1. Supporting Information.

Acknowledgements
The authors are grateful to all anonymous reviewers for their valuable comments and constructive suggestions.

Authors' contributions
Dan Zhou: Writing - editing, conceptualization, formal analysis, funding acquisition; Xingyue Bao: Writing - original draft, data curation; Zhe Chen: Writing—review and editing; Rui Liu: Data collection and analysis; Mingzheng Huang: Software, investigation; Yonglian Xia: investigation, Chao Li: investigation; Yi Huang: Conceptualization, funding acquisition. All authors read and approved the final manuscript.

Funding
This work was financially supported by the National Natural Science Foundation of China (42007344), the Sichuan Science and Technology Program (2023NSFSC0811, 2021JDTD0013, 2021YFQ0066), the Everest Scientific Research Program (2020ZF11405), and the State Key Laboratory of Geohazard Prevention and Geoenvironment Protection Open Fund (SKLGP2022K025).

Availability of data and materials
The data that support the findings of this study are available from the corresponding author upon request.

Declarations

Ethics approval and consent to participate
Not applicable.

Competing interests
The authors declare that they have no known competing financial interests or personal relationships that could have appeared to influence the work reported in this paper.

Author details
[1]State Environmental Protection Key Laboratory of Synergetic Control and Joint Remediation for Soil & Water Pollution, College of Ecology and Environment, Chengdu University of Technology, 610059 Chengdu, China. [2]State Key Laboratory of Geohazard Prevention and Geoenvironment Protection, Chengdu University of Technology, 610059 Chengdu, China. [3]College of Geosciences, Chengdu University of Technology, 610059 Chengdu, China.

Received: 23 September 2022 Revised: 13 February 2023 Accepted: 18 February 2023
Published online: 06 March 2023

References

Balaz M (2018) Ball milling of eggshell waste as a green and sustainable approach: a review. Adv Colloid Interface Sci 256:256–275. https://doi.org/10.1016/j.cis.2018.04.001
Beesley L, Moreno-Jimenez E, Gomez-Eyles JL, Harris E, Robinson B, Sizmur T (2011) A review of biochars' potential role in the remediation, revegetation and restoration of contaminated soils. Environ Pollut 159(12):3269–3282. https://doi.org/10.1016/j.envpol.2011.07.023
Bradford SA, Torkzaban S, Leij F, Simunek J (2015) Equilibrium and kinetic models for colloid release under transient solution chemistry conditions. J Contam Hydrol 181:141–152. https://doi.org/10.1016/j.jconhyd.2015.04.003
Cao G, Sun J, Chen M, Sun H, Zhang G (2021) Co-transport of ball-milled biochar and Cd2 + in saturated porous media. J Hazard Mater 416. https://doi.org/10.1016/j.jhazmat.2021.125725
Chen M, Wang D, Yang F, Xu X, Xu N, Cao X (2017) Transport and retention of biochar nanoparticles in a paddy soil under environmentally-relevant solution chemistry conditions. Environ Pollut 230:540–549. https://doi.org/10.1016/j.envpol.2017.06.101
Debrassi A, Correa AF, Baccarin T, Nedelko N, Slawska-Waniewska A, Sobczak K, Dluzewski P, Greneche J-M, Rodrigues CA (2012) Removal of cationic dyes from aqueous solutions using N-benzyl-O-carboxymethylchitosan magnetic nanoparticles. Chem Eng J 183:284–293. https://doi.org/10.1016/j.cej.2011.12.078
Doherty J (2015) Calibration and uncertainty analysis for complex environmental models. Watermark numerical computing, Brisbane, Australia
Gui X, Song B, Chen M, Xu X, Ren Z, Li X, Cao X (2021) Soil colloids affect the aggregation and stability of biochar colloids. Sci Total Environ 771:145414. https://doi.org/10.1016/j.scitotenv.2021.145414
Haider FU, Coulter JA, Cheema SA, Farooq M, Wu J, Zhang R, Shuaijie G, Liqun C (2021) Co-application of biochar and microorganisms improves soybean performance and remediate cadmium-contaminated soil. Ecotoxicol Environ Saf 214. https://doi.org/10.1016/j.ecoenv.2021.112112
Huang J, Wu Z, Chen L, Sun Y (2015) Surface complexation modeling of adsorption of cd(II) on graphene oxides. J Mol Liq 209:753–758. https://doi.org/10.1016/j.molliq.2015.06.047
Huang X, Chen T, Zou X, Zhu M, Chen D, Pan M (2017) The adsorption of cd(II) on Manganese Oxide investigated by batch and modeling techniques. Int J Environ Res Public Health 14(10). https://doi.org/10.3390/ijerph14101145
Jacques D, Simunek J, Mallants D, van Genuchten MT (2008) Modelling coupled water flow, solute transport and geochemical reactions affecting heavy metal migration in a podzol soil. Geoderma 145(3–4):449–461. https://doi.org/10.1016/j.geoderma.2008.01.009
Jin R, Liu Y, Liu G, Liu L, Zhou J (2020) Influence of chromate adsorption and reduction on transport and retention of biochar colloids in saturated porous media. Colloids Surf A: Physicochem Eng Asp 597. https://doi.org/10.1016/j.colsurfa.2020.124791
Kuzyakov Y, Bogomolova I, Glaser B (2014) Biochar stability in soil: decomposition during eight years and transformation as assessed by compound-specific C-14 analysis. Soil Biol Biochem 70:229–236. https://doi.org/10.1016/j.soilbio.2013.12.021
Lehmann J, Rillig MC, Thies J, Masiello CA, Hockaday WC, Crowley D (2011) Biochar effects on soil biota - A review. Soil Biol Biochem 43(9):1812–1836. https://doi.org/10.1016/j.soilbio.2011.04.022
Liang Y, Bradford SA, Šimůnek J, Klumpp E (2019) Mechanisms of graphene oxide aggregation, retention, and release in quartz sand. Sci Total Environ 656:70–79. https://doi.org/10.1016/j.scitotenv.2018.11.258
Liu G, Zheng H, Jiang Z, Zhao J, Wang Z, Pan B, Xing B (2018) Formation and physicochemical characteristics of nano biochar: insight into chemical and colloidal stability. Environ Sci Technol 52(18):10369–10379. https://doi.org/10.1021/acs.est.8b01481
Liu Y, Sun H, Sun J, Meng X, Jiang Y, Wang N (2021) Transport of micro/nano biochar in quartz sand modified by three different clay minerals. Environ Pollut Bioavailab 33(1):113–121. https://doi.org/10.1080/26395940.2021.1932605
Lu H, Zhang W, Yang Y, Huang X, Wang S, Qiu R (2012) Relative distribution of Pb2 + sorption mechanisms by sludge-derived biochar. Water Res 46(3):854–862. https://doi.org/10.1016/j.watres.2011.11.058
Ma H, Wei M, Wang Z, Hou S, Li X, Xu H (2020) Bioremediation of cadmium polluted soil using a novel cadmium immobilizing plant growth promotion strain Bacillus sp. TZ5 loaded on biochar. J Hazard Mater 388. https://doi.org/10.1016/j.jhazmat.2020.122065
Park CM, Han J, Chu KH, Al-Hamadani YAJ, Her N, Heo J, Yoon Y (2017) Influence of solution pH, ionic strength, and humic acid on cadmium adsorption onto activated biochar: experiment and modeling. J Ind Eng Chem 48:186–193. https://doi.org/10.1016/j.jiec.2016.12.038
Qu X, Fu H, Mao J, Ran Y, Zhang D, Zhu D (2016) Chemical and structural properties of dissolved black carbon released from biochars. Carbon 96:759–767. https://doi.org/10.1016/j.carbon.2015.09.106

Roberts TL (2014) Cadmium and phosphorous fertilizers: the issues and the Science. Procedia Eng 83:52–59. https://doi.org/10.1016/j.proeng.2014.09.012
Robinson T, McMullan G, Marchant R, Nigam P (2001) Remediation of dyes in textile effluent: a critical review on current treatment technologies with a proposed alternative. Bioresour Technol 77(3):247–255. https://doi.org/10.1016/S0960-8524(00)00080-8
Shang J, Liu C, Wang Z (2013) Transport and retention of engineered nanoporous particles in porous media: Effects of concentration and flow dynamics. Colloids Surf A: Physicochem Eng Asp 417:89–98. https://doi.org/10.1016/j.colsurfa.2012.10.030
Shen C, Li B, Huang Y, Jin Y (2007) Kinetics of coupled primary- and secondary-minimum deposition of colloids under unfavorable chemical conditions. Environ Sci Technol 41(20):6976–6982. https://doi.org/10.1021/es070210c
Šimůnek J, He C, Pang L, Bradford SA (2006) Colloid-facilitated solute transport in variably saturated porous media. Vadose Zone J 5(3):1035. https://doi.org/10.2136/vzj2005.0151
Spokas KA, Novak JM, Masiello CA, Johnson MG, Colosky EC, Ippolito JA, Trigo C (2014) Physical disintegration of Biochar: an overlooked process. Environ Sci Technol Lett 1(8):326–332. https://doi.org/10.1021/ez500199t
Sun J, Fan Q, Ma J, Cui L, Quan G, Yan J, Wu L, Hina K, Abdul B, Wang H (2020) Effects of biochar on cadmium (cd) uptake in vegetables and its natural downward movement in saline-alkali soil. Environ Pollut Bioavailab 32(1):36–46. https://doi.org/10.1080/26395940.2020.1714487
Sun Y, Zhang Z, Heng J, Gao C, Jin Q, Chen Z, Guo Z (2022) Co-transport of U(VI) and colloidal biochar in quartz sand heterogeneous media. Sci Total Environ 816. https://doi.org/10.1016/j.scitotenv.2021.151606
Tadros T (2014) Colloid and interface aspects of pharmaceutical science. In Colloid and interface science in pharmaceutical research and development. Elsevier, p 29–54. https://doi.org/10.1016/B978-0-444-62614-1.00002-8
Tan Z, Yuan S, Hong M, Zhang L, Huang Q (2020) Mechanism of negative surface charge formation on biochar and its effect on the fixation of soil cd. J Hazard Mater 384. https://doi.org/10.1016/j.jhazmat.2019.121370
Tang J, Zhang L, Zhang J, Ren L, Zhou Y, Zheng Y, Luo L, Yang Y, Huang H, Chen A (2020a) Physicochemical features, metal availability and enzyme activity in heavy metal-polluted soil remediated by biochar and compost. Sci Total Environ 701. https://doi.org/10.1016/j.scitotenv.2019.134751
Tang X, Shen H, Chen M, Yang X, Yang D, Wang F, Chen Z, Liu X, Wang H, Xu J (2020b) Achieving the safe use of Cd- and As-contaminated agricultural land with an Fe-based biochar: a field study. Sci Total Environ 706. https://doi.org/10.1016/j.scitotenv.2019.135898
Tong M, Li T, Li M, He L, Ma Z (2020) Cotransport and deposition of biochar with different sized-plastic particles in saturated porous media. Sci Total Environ 713. https://doi.org/10.1016/j.scitotenv.2019.136387
Tu C, Wei J, Guan F, Liu Y, Sun Y, Luo Y (2020) Biochar and bacteria inoculated biochar enhanced cd and cu immobilization and enzymatic activity in a polluted soil. Environ Int 137. https://doi.org/10.1016/j.envint.2020.105576
Wan X, Li C, Parikh SJ (2020) Simultaneous removal of arsenic, cadmium, and lead from soil by iron-modified magnetic biochar. Environ Pollut 261. https://doi.org/10.1016/j.envpol.2020.114157
Wang D, Zhang W, Hao X, Zhou D (2013a) Transport of biochar particles in saturated granular media: effects of pyrolysis temperature and particle size. Environ Sci Technol 47(2):821–828. https://doi.org/10.1021/es303794d
Wang D, Zhang W, Zhou D (2013b) Antagonistic effects of humic acid and iron oxyhydroxide grain-coating on biochar nanoparticle transport in saturated sand. Environ Sci Technol 47(10):5154–5161. https://doi.org/10.1021/es305337r
Wang D, Jin Y, Jaisi DP (2015) Cotransport of hydroxyapatite nanoparticles and hematite colloids in saturated porous media: mechanistic insights from mathematical modeling and phosphate oxygen isotope fractionation. J Contam Hydrol 182:194–209. https://doi.org/10.1016/j.jconhyd.2015.09.004
Wang Y, Zhang W, Shang J, Shen C, Joseph SD (2019) Chemical aging changed aggregation kinetics and transport of biochar colloids. Environ Sci Technol 53(14):8136–8146. https://doi.org/10.1021/acs.est.9b00583
Wang Y, Bradford SA, Shang J (2020) Release of colloidal biochar during transient chemical conditions: the humic acid effect. Environ Pollut 260. https://doi.org/10.1016/j.envpol.2020.114068
Wang M, Hu C, Xu J, Jing X, Rahim HU, Cai X (2021a) Facile combinations of thiosulfate and zerovalent iron synergically immobilize cadmium in soils through mild extraction and facilitated immobilization. J Hazard Mater 407. https://doi.org/10.1016/j.jhazmat.2020.124806
Wang Y, Wang L, Li Z, Yang D, Xu J, Liu X (2021b) MgO-laden biochar enhances the immobilization of Cd/Pb in aqueous solution and contaminated soil. Biochar 3(2):175–188. https://doi.org/10.1007/s42773-020-00080-0
Wang X, Dan Y, Diao Y, Liu F, Wang H, Sang W (2022) Transport and retention of microplastics in saturated porous media with peanut shell biochar (PSB) and MgO-PSB amendment: co-effects of cations and humic acid. Environ Pollut 305. https://doi.org/10.1016/j.envpol.2022.119307
Woolf D, Amonette JE, Street-Perrott FA, Lehmann J, Joseph S (2010) Sustainable biochar to mitigate global climate change. Nat Commun 1. https://doi.org/10.1038/ncomms1053
Xiang L, Liu S, Ye S, Yang H, Song B, Qin F, Shen M, Tan C, Zeng G, Tan X (2021) Potential hazards of biochar: the negative environmental impacts of biochar applications. J Hazard Mater 420:126611. https://doi.org/10.1016/j.jhazmat.2021.126611
Xiao Y, Wang L, Zhao Z, Che Y (2020) Biochar shifts biomass and element allocation of legume-grass mixtures in Cd-contaminated soils. Environ Sci Pollut Res 27(10):10835–10845. https://doi.org/10.1007/s11356-019-07357-3
Xu F, Wei C, Zeng Q, Li X, Alvarez PJJ, Li Q, Qu X, Zhu D (2017) Aggregation behavior of dissolved black carbon: implications for vertical mass flux and fractionation in aquatic Systems. Environ Sci Technol 51(23):13723–13732. https://doi.org/10.1021/acs.est.7b04232
Xu C, Zhao J, Yang W, He L, Wei W, Tan X, Wang J, Lin A (2020) Evaluation of biochar pyrolyzed from kitchen waste, corn straw, and peanut hulls on immobilization of pb and cd in contaminated soil. Environ Pollut 261. https://doi.org/10.1016/j.envpol.2020.114133
Xu Z, Niu Z, Pan D, Zhao X, Wei X, Li X, Tan Z, Chen X, Liu C, Wu W (2021) Mechanisms of bentonite colloid aggregation, retention, and release in saturated porous media: role of counter ions and humic acid. Sci Total Environ 793:148545. https://doi.org/10.1016/j.scitotenv.2021.148545
Yang W, Wang Y, Shang J, Liu K, Sharma P, Liu J, Li B (2017) Antagonistic effect of humic acid and naphthalene on biochar colloid transport in saturated porous media. Chemosphere 189:556–564. https://doi.org/10.1016/j.chemosphere.2017.09.060
Yang W, Bradford SA, Wang Y, Sharma P, Shang J, Li B (2019) Transport of biochar colloids in saturated porous media in the presence of humic substances or proteins. Environ Pollut 246:855–863. https://doi.org/10.1016/j.envpol.2018.12.075
Yang W, Feng T, Flury M, Li B, Shang J (2020a) Effect of sulfamethazine on surface characteristics of biochar colloids and its implications for transport in porous media. Environ Pollut 256. https://doi.org/10.1016/j.envpol.2019.113482
Yang W, Shang J, Li B, Flury M (2020b) Surface and colloid properties of biochar and implications for transport in porous media. Crit Rev Env Sci Technol 50(23):2484–2522. https://doi.org/10.1080/10643389.2019.1699381
Yang W, Qu T, Flury M, Zhang X, Gabriel S, Shang J, Li B (2021) PAHs sorption to biochar colloids changes their mobility over time. J Hydrol 603. https://doi.org/10.1016/j.jhydrol.2021.126839
Yu Y, Murthy BN, Shapter JG, Constantopoulos KT, Voelcker NH, Ellis AV (2013) Benzene carboxylic acid derivatized graphene oxide nanosheets on natural zeolites as effective adsorbents for cationic dye removal. J Hazard Mater 260:330–338. https://doi.org/10.1016/j.jhazmat.2013.05.041
Zhang W, Niu J, Morales VL, Chen X, Hay AG, Lehmann J, Steenhuis TS (2010) Transport and retention of biochar particles in porous media: effect of pH, ionic strength, and particle size. Ecohydrology 3(4):497–508. https://doi.org/10.1002/eco.160
Zhang H, Lu T, Shang Z, Li Y, He J, Liu S, Li D, Zhou Y, Qi Z (2020) Transport of Cd2 + through saturated porous media: insight into the effects of low-molecular-weight organic acids. Water Res 168. https://doi.org/10.1016/j.watres.2019.115182
Zhu S, Zhao W, Wang P, Zhao L, Jin C, Qiu R (2021) Co-transport and retention of zwitterionic ciprofloxacin with nano-biochar in saturated porous media: impact of oxidized aging. Sci Total Environ 779. https://doi.org/10.1016/j.scitotenv.2021.146417